sustainability

MDPI

Article

Performance Enhancement of Solar Still Unit Using v-Corrugated Basin, Internal Reflecting Mirror, Flat-Plate Solar Collector and Nanofluids

Mostafa AbdEl-Rady Abu-Zeid [1], Yasser Elhenawy [2,3,4], Monica Toderaș [5,*], Mohamed Bassyouni [4,6,7], Thokozani Majozi [3,*], Osama A. Al-Qabandi [8] and Sameh Said Kishk [1]

1 Department of Agricultural Engineering, Faculty of Agriculture, Suez Canal University, Ismailia 41522, Egypt; mostafa241981@agr.suez.edu.eg (M.A.-R.A.-Z.); sameh_kishk@agr.suez.edu.eg (S.S.K.)
2 Department of Mechanical Power Engineering, Faculty of Engineering, Port Said University, Port Said 42526, Egypt; yasser.elhenawy@wits.ac.za
3 School of Chemical and Metallurgical Engineering, University of the Witwatersrand, 1 Jan Smuts Avenue, Johannesburg 2000, South Africa
4 Center of Excellence in Membrane-Based Water Desalination Technology for Testing and Characterization (CEMTC), Port Said University, Port Said 42526, Egypt; m.bassyouni@eng.psu.edu.eg
5 Faculty of Sciences, Oradea University, Universităţii Street No. 1, 410087 Oradea, Romania
6 Department of Chemical Engineering, Faculty of Engineering, Port Said University, Port Said 42526, Egypt
7 Faculty of Industry and Energy, East Port Said University of Technology, North Sinai 45632, Egypt
8 College of Engineering and Technology, American University of the Middle East, Egaila 54200, Kuwait; osamah.alqabandi@aum.edu.kw
* Correspondence: monicatoderas@gmail.com (M.T.); thokozani.majozi@wits.ac.za (T.M.)

Abstract: The conventional solar still (CSS) unit faces challenges such as low productivity (P_d) and thermal efficiency (η_{th}) due to the limited temperature difference between the hot water and the cold interior glass cover surfaces ($\Delta T_{w\text{-}gi}$). This study addresses these issues by introducing enhancements in the CSS unit, incorporating a v-corrugated-type basin, internal reflecting mirror, flat-plate solar collector (FPSC) still, and FPSC nanofluids. A v-corrugated-type basin, internal reflecting mirror, FPSC still, and FPSC nanofluids elicited a significant improvement in the distillate productivity (P_d) up to approximately 22.39%, 41.72%, 70.10%, and 104.13% compared to the CSS unit. This increase in the P_d is attributed mainly to a notable raise in the $\Delta T_{w\text{-}gi}$, showing increments of around 34.33%, 52.32%, 77.37%, and 112.87% compared to the CSS unit. Moreover, a v-corrugated basin, internal reflecting mirror, FPSC still, and FPSC nanofluids substantially increased the average daily thermal efficiency (η_{th}), around 22.01%, 26.71%, 39.57%, and 56.21%, respectively. The results confirmed that integrating the v-corrugated basin, internal reflecting mirror, FPSC still, and FPSC nanofluids within a combined seawater distillation system can significantly enhance the performance of the CSS unit. These different combinations effectively raised the basin water temperature (T_w) and $\Delta T_{w\text{-}gi}$, consequently improving the overall performance of the solar still unit.

Keywords: solar still; reflector; solar thermal collector; v-corrugated-type basin; nanofluids

Citation: Abu-Zeid, M.A.-R.; Elhenawy, Y.; Toderaș, M.; Bassyouni, M.; Majozi, T.; Al-Qabandi, O.A.; Kishk, S.S. Performance Enhancement of Solar Still Unit Using v-Corrugated Basin, Internal Reflecting Mirror, Flat-Plate Solar Collector and Nanofluids. *Sustainability* **2024**, *16*, 655. https://doi.org/10.3390/su16020655

Academic Editor: Simon Pezzutto

Received: 12 November 2023
Revised: 25 December 2023
Accepted: 8 January 2024
Published: 11 January 2024

1. Introduction

Solar still (SS) is a thermal desalination unit driven by a temperature difference between the two hot water and cold interior glass cover surfaces ($\Delta T_{w\text{-}gi}$) [1]. Utilizing water desalination through solar collectors can aid in mitigating the spread of diseases such as COVID-19 by providing a more reliable and clean water source, reducing reliance on potentially contaminated water supplies [2]. The evaporation and condensation were gathered in an integrated system [1], as shown in Figure 1. Comparing with other thermal desalination processes, such as humidification-dehumidification (HDH), vapor compression (VC), multi-stage flash (MSF), and multi-effect distillation (MED), the solar still (SS) is

a more convenient water desalination system utilized at remote coastal regions owing to low operation and maintenance costs, low-operating temperatures, easy operation process, no need for skilled workers, and less energy use, where it depends only upon the incident solar radiation [2].

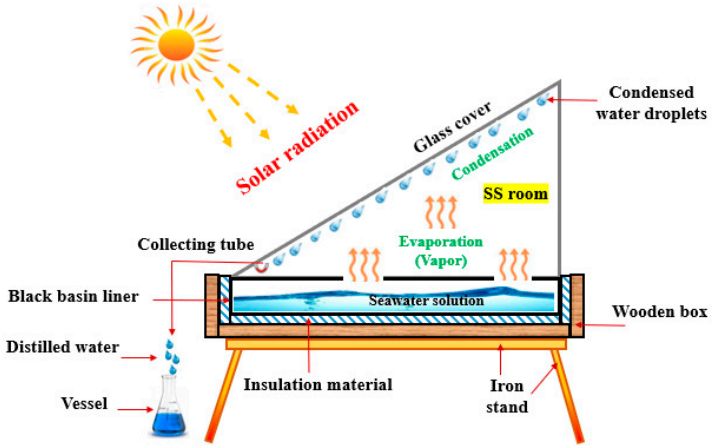

Figure 1. Solar still.

The increasing or decreasing $\Delta T_{w\text{-}gi}$ deeply affects the solar still distillate productivity (P_d) [3], whereas, the increase in the $\Delta T_{w\text{-}gi}$ helps in upgrading the still distillate productivity (P_d) and vice versa [4]. The single slope-type solar still is one of the most common solar desalination units [5]; however, low distillate productivity (P_d) ranging between 2 and 5 L/m^2/day has been challenging [6]. To solve this issue, the water temperature (T_w) in the still basin at first and the $\Delta T_{w\text{-}gi}$ should be augmented. This objective could be accomplished practically by linking a flat-plate solar thermal collector (FPSC) with a solar distillation unit in a system named FPSC still [7], fixing an internal reflecting mirror to the still glass cover [8], and replacing a flat-plate type still basin with a v-corrugated-type still basin [9].

Eltawil and Omara [10] stated that the FPSC still noticeably enhanced the still distillate productivity (P_d) by about 56% and 82% in the case of sprayed hot water (passive and active recirculation modes) and by 76% in the case of jet hot water (active recirculation mode). Also, Sheeba et al. [11] demonstrated that a combined active desalination system (FPSC still) outperformed the passive desalination system (solar still operating alone) in terms of the daily thermal efficiency (η_{th}) by around 20.4% and 23.6% for tap and saline water, respectively. Likewise, the distillate productivity (P_d) of the FPSC still was greater by 24% compared with the passive desalination system [12]. Similarly, Badran and Al-Tahaineh [13] and Badran [14] announced an around 36% enhancement in the distillate productivity (P_d) of the active system compared to the passive one.

As for a reflector, a work was proceeded by Tanaka [15]; during the winter season, a noticeable improvement in the still distillate productivity (P_d) from 70% to 100% resulted due to the positive influence of internal and external reflectors, respectively. Hiroshi and Yasuhito [16] investigated the impact of reflectors (internal and external) on the single slope solar still productivity (P_d). The obtained outcomes showed the positive effect of reflectors in enhancing the overall still distillate productivity (P_d), by around 21%. The authors also recommended the inclination of a single slope solar still and reflector for fulfilling better performance throughout the year. As described by Omara et al. [17], a comparative investigation was carried out between the stepped solar still unit and the conventional one. The results demonstrated that the stepped still unit remarkably outperforms the conventional one. The distillate productivity (P_d) of the stepped still with fixing top and bottom reflectors was upgraded by approximately 125% compared to the conventional still. Another comparative investigation by Omara et al. [18] demonstrated that a v-corrugated-type still basin with wick and internal reflecting mirrors achieved better productivity (P_d)

than that of the conventional one by about 145.5%. Similarly, Al-Hayek and Badran [6] reported an increment of 20% in the productivity (P_d) of asymmetric greenhouse-type stills compared to the symmetric greenhouse-type still. Furthermore, Abdallah et al. [19] reported that the distillate productivity (P_d) for the modified single slope solar still with reflecting mirrors fixed on all interior sides was maximal at about 30% compared to the productivity (P_d) without mirrors.

A v-corrugated-type still basin promoted the solar still performance as a result of increasing the surface area of heat and mass transferring from the hot water surface to the cold interior glass cover surface. Omara et al. [9] compared the volume of the still distillate productivity (P_d) for three different kinds of absorber plate still basin, such as finned, corrugated, and flat shapes. The experimental results showed a remarkable improvement in productivity (P_d) in the case of finned and v-corrugated-type still basins in comparison with the flat-plate type still basin, reaching around 40% and 21%, respectively.

By using several kinds of nanofluids, the solar collector's absorption efficiency can be enhanced [20]. In order to produce distilled water, experimental work was conducted to study the flat-plate and evacuated-tube collectors [21]. The physical characteristics of nanofluids and the yield of distilled water at various seawater flow rates were determined. In the presence of carbon nanotubes in paraffin wax and ethylene glycol nanofluids, the desalination unit's performance was assessed. Ethylene glycol nanofluid at 80–100 °C increased the flat-plate collector's evaporation efficiency by up to 36%.

The pressure drops and thermal efficiency of several nanofluids inside a flat-plate solar collector were computed. The thermal efficiency for Al_2O_3/water, however, was examined both experimentally and numerically [22]. Working fluids include CuO/water, Al_2O_3/water, Ti_2O/water, and Si_2O/water nanofluids, with vol. concentrations of 1, 2, and 3%, respectively. As the volume concentration of nanofluid rises, thermal efficiency does as well. For instance, 2% Al_2O_3/water has a thermal efficiency that is 5.3% higher and 29.75% more than 1% Al_2O_3/water and water. The thermal efficiencies of CuO and Al_2O_3 are 46% and 43.8%, respectively, assuming a uniform mass flow rate and 1% volume concertation.

Previous studies focused on specific enhancements or modifications individually, lacking a comprehensive approach that combines multiple innovations to maximize efficiency and productivity. Many studies did not extensively address the influence of varying environmental conditions on the performance of enhanced solar distillation systems, thereby limiting the broader applicability of their findings. A few studies conducted detailed comparative analyses between different enhancement methods or their combined effects to understand their synergistic impact comprehensively. The scalability and adaptability of enhancements across diverse geographical regions or varying water salinity levels were not extensively addressed in some studies, limiting their broader applicability [21–23].

The novelty of this study lies in its comprehensive approach that integrates multiple enhancements (v-corrugated basin, internal reflecting mirror, FPSC still, and FPSC nanofluids) into a single solar distillation system. This approach could potentially address various limitations observed in previous studies. The study offers a comparative evaluation of various enhancements in terms of their individual and combined impact on distillate productivity and thermal efficiency. This comparative analysis provides valuable insights into the synergistic effects of these enhancements. By emphasizing performance improvements in a combined seawater distillation system, this study aims to bridge the gap between theoretical advancements and practical application, potentially making it more relevant for real-world scenarios. The significant improvements reported in distillate productivity (P_d) and average daily thermal efficiency (η_{th}) due to these combined enhancements underscore the novelty of this study. This study potentially addresses environmental dependency concerns by assessing the performance enhancements under varying conditions, making the findings more robust and applicable in diverse settings.

2. Thermal Analysis

The following assumptions were used in the present analytical analysis [22]:

- The glass cover has the same area A_g as the water film A_w.
- The water film and the glass cover are gray surfaces.
- The water film is maintained at a constant temperature T_w.
- The glass cover is taken at a constant temperature T_{gi}.
- There is constant and equal specific heat C for feed, brine, and distillate.
- The sky can be considered as a black body.
- The glass cover is exposed only to the sky.

The energy flow and energy balance for the solar still unit are given by Equations (1) and (2) [23].

- Heat balance for the still basin (b)

$$m_b\, C_{pb}\, \frac{dT_b}{dt} \;=\; IA_b \;-\; q_{bwb} \;-\; q_b \tag{1}$$

- Heat balance for water in the basin (w)

$$m_w\, C_{pw}\, \frac{dT_w}{dt} \;=\; I\, A_w \;+\; q_{bw} \;-\; q_{rw} \;-\; q_{cw} \;-\; q_{ew} \tag{2}$$

- Heat balance for the glass cover (g) can be determined using Equation (3).

$$m_g\, C_{pg}\, \frac{dT_g}{dt} \;=\; I\, A_g \;+\; q_{rw} \;+\; q_{cw} \;+\; q_{ew} \;-\; q_{cga} \;-\; q_{rgs} \tag{3}$$

- The condensate rate is given by Equation (4) [23].

$$\frac{dm_c}{dt} \;=\; \frac{h_{ew}\, A_b\, (T_w \;-\; T_{gi})}{L_w} \;=\; \frac{q_{ew}}{L_w} \tag{4}$$

The rate of heat transfer through convection, denoted as q_{cw} (W), within the solar still, specifically from the water surface to the interior surface of the glass cover, is described by Equation (5) [24].

$$q_{cw} \;=\; h_{cw}\, A_b\, (T_w \;-\; T_{g_i}) \tag{5}$$

where T_w and T_{gi} are water temperature and temperature of the glass interior surface (K), respectively. Meanwhile, h_{cw} is the convective heat transfer coefficient in ($\mathrm{Wm^{-2}\,K^{-1}}$); it is given by Equation (6) [25].

$$h_{cw} = \; 0.884 \left[(T_w \;-\; T_{g_i}) \;+\; \frac{(P_w \;-\; P_{gi})}{268900 \;-\; P_w}\, (T_w + \;273) \right]^{1/3} \tag{6}$$

where P_w and P_{gi} are the partial pressures in ($\mathrm{Nm^{-2}}$) for water vapor at water and the interior glass surface temperatures within the still, which are given by Equations (7) and (8) [26].

$$P_w \;= exp \left[25.317 \;-\; \left(\frac{5144}{T_w \;+\; 273} \right) \right] \tag{7}$$

$$P_{gi} = \; exp \left[25.317 - \left(\frac{5144}{T_{gi} + 273} \right) \right] \tag{8}$$

Rate of the evaporative heat transfer within the still from the water surface to the inner glass cover surface, which is denoted by q_{ew} in (W) units in Equation (3), can be determined using Equation (9).

$$q_{ew} \;=\; h_{ew}\, A_b\, (T_w \;-\; T_{gi}) \tag{9}$$

where the evaporative heat transfer coefficient, h_{ew} in (Wm^{-2} K^{-1}), is given by Equation (10) [23].

$$h_{ew} = 16.273 \times 10^{-3} h_{cw} \frac{(P_w - P_{gi})}{(T_w - T_{gi})} L_w \quad (10)$$

The rate of radiative heat transfer from the water surface to the interior surface of the glass cover, q_{rwb} in (W) in Equation (3), is given by Equation (11).

$$q_{rw} = h_{rw} A_b (T_w - T_{gi}) \quad (11)$$

where h_{rw} is the radiative heat transfer coefficient in (Wm^{-2} K^{-1}). It can be determined using Equation (12).

$$h_{rw} = \frac{\varepsilon_{eff} \sigma \left[(T_w + 273)^4 - (T_{gi} + 273)^4\right]}{(T_w - T_{gi})} \quad (12)$$

where ε_{eff} is the effective emissivity factor of diffuse radiation from the water surface to the interior surface of the glass cover and σ is the Stefan–Boltzmann constant taken as 56.7×10^{-9} Wm^{-2} K^{-4} [27]. If the shape factor is taken as the unity and the emissivity of the water is 0.90, the radiative heat transfer from the hot water surface to the interior surface of the glass cover can be determined using Equation (13).

$$q_{rw} = 0.90 A_b \sigma \left[(T_w + 273)^4 - (T_{gi} + 273)^4\right] \quad (13)$$

Thus, the internal heat transfer within the still is governed by three modes: the heat exchange between condensing and evaporating surfaces, i.e., from water surface to interior surface of glass cover of the solar still, which is known as internal heat transfer. These modes are radiation, convection, and evaporation, and, hence, the total internal heat transfer coefficient (h_1) from the water surface to the interior surface of the glass cover will be the sum of all these modes of heat transfer coefficients according to Tiwari and Tiwari [28], as given in Equation (14).

$$h_1 = h_{cw} + h_{ew} + h_{rw} \quad (14)$$

And the total value of the energy transfer q_1 in (W) within the solar still from the water surface to the interior surface of the glass cover can be obtained using Equation (15).

$$q_1 = q_{cw} + q_{ew} + q_{rw} \quad (15)$$

The influence of relative magnitudes of these three modes can be better understood by evaluating the fraction of total energy, as performed by Cooper [29]. These convective (F_c), evaporative (F_e), and radiative (F_r) fractions can be determined using Equation (16) [30].

$$F_c = \frac{q_{cw}}{q_1} F_e = \frac{q_{ew}}{q_1} F_r = \frac{q_{rw}}{q_1} \quad (16)$$

q_{bw} in (W) in Equation (2) represents the rate of the convective heat transfer coefficient from the black basin liner (the hottest region in the still) to the water surface. The calculations were performed by applying Equation (17).

$$q_{bw} = h_{bw} A_b (T_{bi} - T_w) \quad (17)$$

where T_{bi} is the inner basin temperature (K) and h_{bw} is the convective heat transfer coefficient from the black basin liner to the water surface in (Wm^{-2} K^{-1}).

The conductive heat transfer coefficient (U_g) through the thickness of the still glass cover (x_g) could be formulated, as given in Equation (18).

$$U_g = k_g / x_g \tag{18}$$

where k_g and x_g are the thermal conductivity for the glass cover in ($Wm^{-1}\ K^{-1}$) and the glass cover thickness in (m), respectively.

The rate of heat transfer from the exterior surface of the glass cover to the surroundings due to convection, q_{cga} in (W) (caused by the wind), is given by Equation (19).

$$q_{cga} = h_{cga}\ A_g\ (T_{go} - T_{ao}) \tag{19}$$

where T_{go}, T_{ao}, and h_{cga} are the outer glass cover temperature, ambient air temperature, and convective heat transfer coefficient, respectively. The convective heat transfer coefficient (h_{cga}) depends on the prevailing wind speed. It is given by Equation (20) [31].

$$h_{cga} = 5.7 + 3.8w \tag{20}$$

where w is the wind speed in (m/s).

The rate of radiative heat transfer from the exterior surface of the glass cover to the sky can be determined using Equation (21).

$$q_{rgs} = h_{rgs} A_g \left(T_{go} - T_{sky}\right) \tag{21}$$

where h_{rgs} is the radiative heat transfer coefficient in ($Wm^{-2}\ K^{-1}$); it is given by Equation (22)

$$h_{rgs} = \frac{\varepsilon_{eff}\ \sigma \left[\left(T_{go} + 273\right)^4 - \left(T_{sky} + 273\right)^4\right]}{\left(T_{go} - T_{sky}\right)} \tag{22}$$

where ε_{eff} is the effective emissivity factor of diffuse radiation from the exterior surface of the glass cover to the sky and σ is the Stefan–Boltzmann constant taken as $56.7 \times 10^{-9}\ Wm^{-2}\ K^{-4}$. If the shape factor is taken as unity and the emissivity of the glass cover is 0.90, the radiative heat transfer from the exterior surface of the glass cover to the sky can be determined using Equation (23).

$$q_{rgs} = 0.90\ \sigma A_g \left[\left(T_{go} + 273\right)^4 - \left(T_{sky} + 273\right)^4\right] \tag{23}$$

where T_{sky} is the sky temperature and, generally, the average sky temperature during the operating hours is given by Equation (24) [32].

$$T_{sky} = 0.0552\ T_{ao}^{1.5} \tag{24}$$

The total external heat transfer coefficient (h_2) is given by Equation (25).

$$h_2 = h_{cga} + h_{rgs} \tag{25}$$

The total value of the rate of energy transfer from the exterior surface of the glass cover to its surroundings q_2 in (W) can be determined using Equation (26).

$$q_2 = q_{cga} + q_{rgs} \tag{26}$$

Hence, the overall heat transfer coefficient (U_t) through the top of the still can be calculated using Equation (27).

$$U_t^{-1} = (h_1)^{-1} + \left(x_g / k_g\right) + (h_2)^{-1} \tag{27}$$

The rate of conductive heat losses q_b in (W) from the basin bottom to the atmosphere can be formulated using Equation (28) [33,34].

$$q_b = \frac{k_{in}}{x_{in}} (T_{wb} - T_{amb}) \quad (28)$$

where k_{in} and X_{in} are the insulation thermal conductivity in (Wm^{-1} K^{-1}) and the basin thickness in (m), respectively.

3. Materials and Methods

Experimental comparison of the conventional solar still (CSS) and modified solar still (MSS) performance for seawater desalination was implemented during August 2023 at a latitude of (30°35′00″ N 32°16′00″ E). The conventional solar still (CSS) is used in this work as a reference unit for a comparison with other modified solar still (MSS) units.

Each and every chemical element used in the experimental testing was of reagent grade. Commercial Al_2O_3 nanoparticles with a 99.99% purity rating and an average diameter of 45 nm were acquired from Sigma-Aldrich GmbH and placed in the base fluid. Aluminum oxide nanofluid was chosen because of its superior Brownian motion, thermal conductivity of higher effective, lower density, and ability to decrease sedimentation [35]. In order to disperse Al_2O_3 along the base fluid, distilled water, and to increase the stability of Al_2O_3/seawater nanofluid, sodium dodecyl benzene sulfonate was used as a natural surfactant [36]. Sodium dodecyl benzene sulfonate supplied the optimum stability level for the Al_2O_3-seawater nanofluid. The Al_2O_3 nanoparticles were dispersed in water using sonicator for 30 min in an ultrasonic bath at 3% (w/v). Model USC-1400 was used at 40 kHz of ultrasound frequency. The Malvern Panalytical pro blue unite (Malvern Instruments, Malvern, UK) was used to measure the zeta potential of particles in a liquid. Zeta potential is an electric potential that exists at the interface between a particle surface and the liquid medium in which it is dispersed. It is a key parameter in understanding and controlling the stability of colloidal dispersions. The Zetasizer primarily uses a technique known as electrophoretic light scattering (ELS). In this method, a laser beam was directed through a sample containing dispersed particles. The instrument applies an electric field to the sample, causing charged particles to move. The velocity of these moving particles is related to their zeta potential. The velocity data are then used to calculate the zeta potential of the particles based on the Smolu–Chowski equation, which relates the electrophoretic mobility of the particles to the zeta potential. The Zetasizer provides results in terms of zeta potential, which indicates the magnitude and direction of the electric charge on the particles' surfaces. This information is crucial for understanding the stability of colloidal systems. Water and nanoparticles' physical characteristics are listed in Table 1.

Table 1. Al_2O_3 nanoparticles' and water's physical characteristics.

	Density, kg/m^3	Specific Heat, J/kg K	Thermal Conductivity, W/m K	Ref.
Al_2O_3	3995	880	35	[37,38]
seawater	1025	4007	0.60	[37,38]

Density ρ_{nf} and heat capacity C_{nf}, which may differ considerably from those of the base fluid, are the two key nanofluid parameters that are used in the determination of the usable thermal efficiency extracted during the heating process. Authors did not test the density and heat capacity of Al_2O_3 nanofluids at different nanoparticle volume concentrations; thus, the density and heat capacity were calculated using Equations (29)–(31) proposed by Pak and Cho [39] and Xuan and Roetzel [40].

$$\rho_{nf} = (1 - \phi)\rho_{bf} + \phi\, \rho_p \quad (29)$$

$$(\rho \cdot C)_{nf} = (1 - \phi)(\rho \cdot C_p)_{bf} + \phi\ (\rho \cdot C_p)_p \quad (30)$$

where base fluid, nanoparticle, and nanofluid are given the subscriptions *f*, *p*, and *nf*, respectively. Using the Hamilton–Crosser projected model [41], the thermal conductivity K_{nf} of the nanofluid is assessed using Equation (31).

$$Knf/kf = kp + (n - 1)kf + (n - 1)\phi(kp - kf)/kp + (n - 1)kf - \phi(kp - kf) \quad (31)$$

where *n* denotes the particle sphericity and $n = 3$ denotes the particle form factor. The sphericity values for cylinder-shaped and spherical particles are 0.5 and 1, respectively. Due to the spherical shape of the Al_2O_3 nanoparticles, the value of *n* in the current study is, thus, considered to be 3. Table 2 lists the thermophysical characteristics of Al_2O_3 nanofluids as a function of nanoparticle volume concentration.

Table 2. Thermophysical characteristics of nanofluids, particles sizes, and zeta potentials of Al_2O_3/water nanofluid at $\phi = 3\%$.

Property	Value
Volume concentration ϕ, (% vol.)	3
Density ρ, (kg/m^3)	1088
Thermal conductivity *k*, (W/m.K)	0.67
Average particles size, (nm)	45
Zeta potential, (mV)	−27.71

Al_2O_3 nanoparticles acquire a negative charge on their surface due to the presence of hydroxyl (OH-) groups. When dispersed in a water medium, these groups dissociate, resulting in negatively charged surfaces on the nanoparticles. A high negative zeta potential (−27.71 mV), as listed in Table 2, suggested a high degree of electrostatic repulsion between the particles, which helps prevent their agglomeration or aggregation.

This stabilization mechanism is crucial in nanofluid applications because it helps maintain the dispersion stability of nanoparticles in the fluid, preventing them from clumping together and thereby maintaining their desired properties and characteristics, such as uniformity and stability of the nanofluid.

3.1. Experimental Set-Up

The conventional (CSS) and modified solar still (MSS) units utilized in this investigation are shown in Figure 2. The single slope solar still units consisted mainly of seawater tank, glass cover, iron basin, wooden box, circulation water pump, and connection piping. The tested solar still units were erected facing south during the experiments, and the module's inclination was fixed at 30° with respect to the ground to maximize the quantity of sunlight that hit the module's surface. The flat-plate solar thermal collector (FPSC) was used to warm the seawater solution (acts as a thermal carrier) flowing into the copper collector's tube by absorbing the incident solar radiation and transferring heat into seawater stream. The FPSC operated under forced circulation using a 375-Watt water circulation pump. It was placed in the south direction with a slope of 30° to maximize the solar intensity and to transfer the maximum possible solar radiation.

The seawater solution examined in this experiment was characterized with around 33,162 ppm salt concentration. A plastic water tank (50 L capacity and 2 mm thick) was fixed above iron stand to supply the solar still (SS) unit with the required water depth. The thickness of transparent glass cover of solar still is 3 mm, having the same dimensions, as illustrated in Figure 3. It was sealed with silicone rubber to prevent any vapor leakage. The reflective mirror, possessing a thickness of 2 mm, was fixed perpendicular to a still glass surface, demonstrating dimensions of 0.5 m in height and 1.5 m in length.

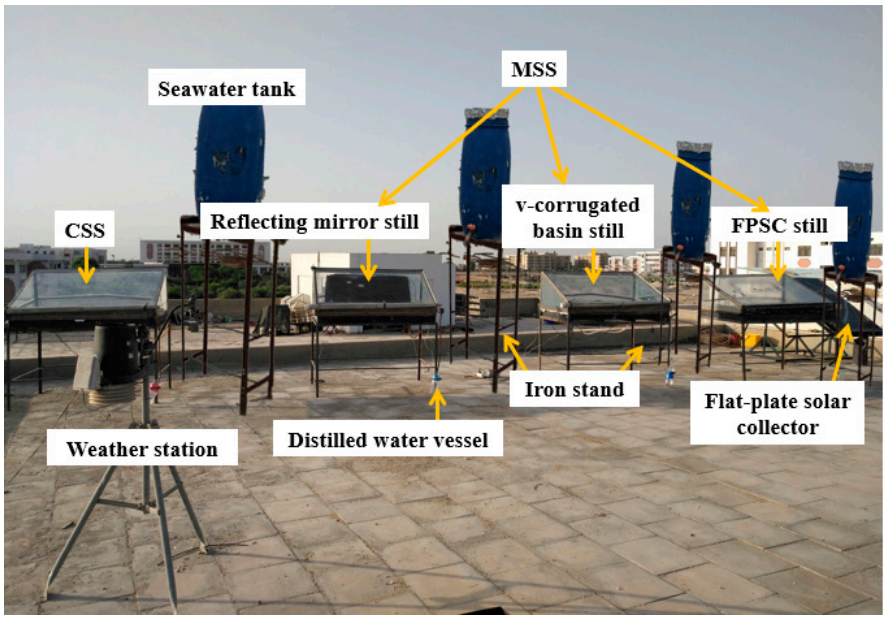

Figure 2. Photograph of experimental set-up.

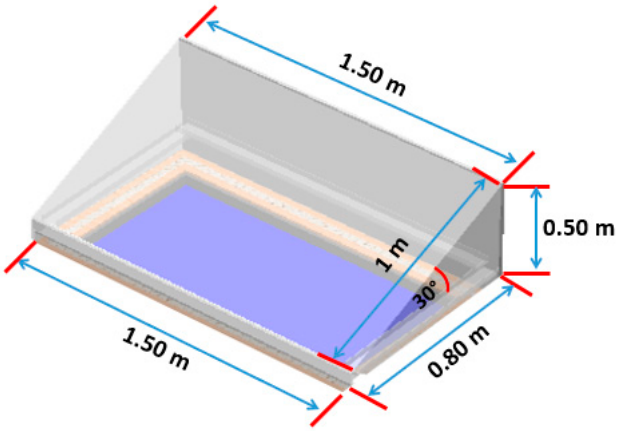

Figure 3. Dimensions of solar still glass cover.

The flat-plate and v-corrugated-type still basins used in this study are illustrated in Figure 4. All still basins are fabricated from galvanized iron with the same outside dimensions of 0.8 m width, 1.3 m length, 0.1 m depth. It should be noted here that the inside surface area of the three solar still units used a flat-plate type basin equal to 1.04 m^2. The basin, designed in a v-corrugated type, measures 0.8 m in width, 2.4 m in length, and stands at a height of 7 cm. This configuration is illustrated in Figure 4. The angle of bending between two successive tops or bottoms is around 60°, and the distance between each two tops or two bottoms is about 8 cm (equilateral triangles) with 7 cm height. This basin consists of 15 tunnels (tops and bottoms of corrugated shape). The depth of seawater inside the still basin is kept at 2 cm during the experiment operating time.

The still basins were painted in black coating to enhance the heat absorption from the sun, and each one is added separately inside a wooden box for low heat loss. A wooden box was made from plywood material with the same outside dimensions of 1.44 × 0.94 m^2 and thickness of 0.025 m. The side spaces between the still basin and the wooden box are filled with Styrofoam (0.07 m thick and 0.04 Wm^{-1} K^{-1} thermal conductivity) and with rock wool at the bottom basin (thick of 0.02 m and 0.0346 Wm^{-1} K^{-1} thermal conductivity). Two openings are made at the side and bottom of still basin for entry and drainage of seawater solution. A tube made of PVC is fixed between the sloped glass cover surface and still basin to collect the water droplets resulting from the vapor condensation. The flat-plate

solar thermal collector (FPSC) utilized as a heat source in this experiment was designed in a rectangular shape, as shown in Figure 5. It consists of black aluminum absorber plate (1 mm thick), serpentine copper tube (26 m tube length, 8 mm diameter, 30 channels with 50 mm pitch between tubes), glass cover surface (3 mm thickness), wooden box (160 cm length, 90 cm width, 10 cm depth, 5 mm thickness, and surface area of 1.44 m^2), and insulation material.

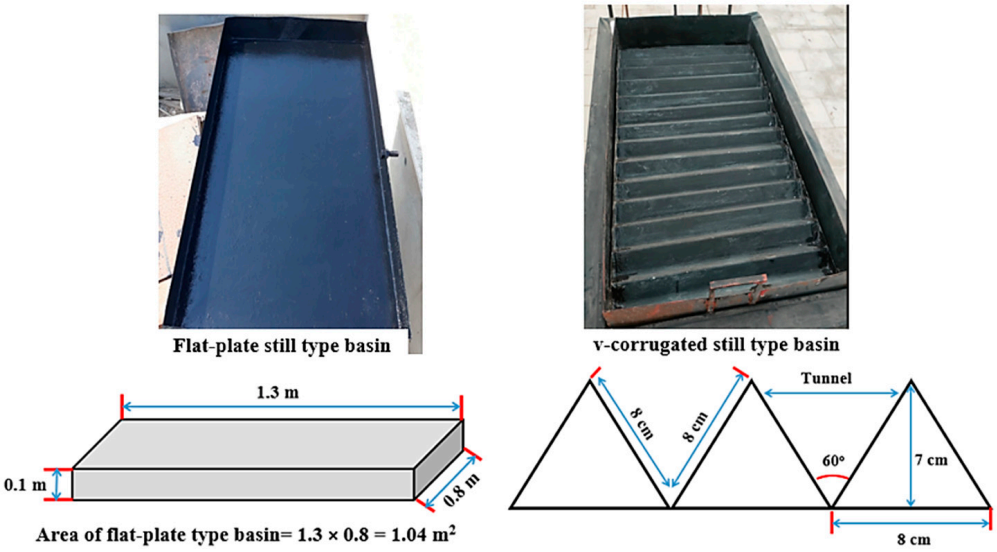

Figure 4. Photograph of flat-plate and v-corrugated-type still basins.

Figure 5. Photograph of flat-plate solar thermal collector (FPSC).

3.2. Solar Still Configurations

In the current experiment, as elucidated schematically in Figure 6, the cold seawater solution (pointing out as a blue solid line in the figure) flowed from the feeding tank to the iron basin after opening the control valve (7). The control valve (7) was left open until the still basin filled up with cold seawater solution at the required depth; then, it closed to prevent more water flowing into the basin. After that, the cold seawater solution in the basin began to warm up and convert to a hot solution (red solid line in the figure) by the solar rays transmitted through the glass cover surface and absorbed by the linear black basin. The hot seawater solution starts to evaporate and produce a vapor at the hot water surface to remove salts. After that, the generated vapor molecules transferred by a convection mode towards the interior cold glass cover surface. Then, it condensed and turned into pure water droplets. The water droplets moved down on the interior glass cover surface under a gravitational effect and collected as distilled water in the vessel (green solid line in the figure). To maintain the depth of water constantly in the still basin

during the experiment, the control valve (7) was opened once again to compensate any shortage in water depth as a result of evaporation process.

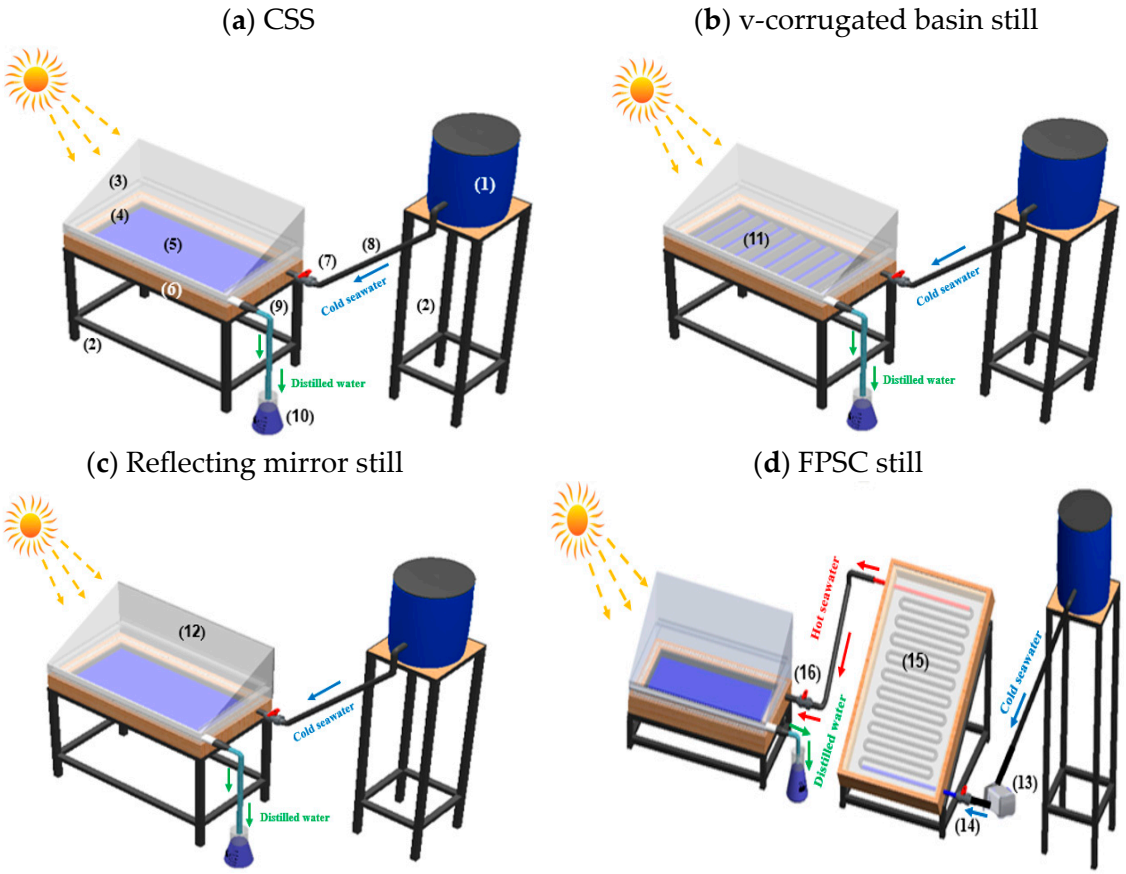

Figure 6. The schematic diagrams illustrating the (**a**) CSS, (**b**) v-corrugated basin still, (**c**) reflecting mirror still and (**d**) FPSC still with and without nanofluids used in this investigation: (1) seawater tank, (2) iron stand, (3) glass cover, (4) flat-plate-type still basin, (5) seawater, (6) wooden box, (7) control valve (1), (8) connecting pipe, (9) distillate PVC tube, (10) distilled water vessel (11) v-corrugated-type still basin, (12) reflecting mirror, (13) water pump, (14) control valve (2), (15) flat-plate solar thermal collector, (16) control valve (3).

The same steps were repeated in case of solar still (SS) unit equipped with a solar thermal collector with (FPSC nanofluid) and without nanofluids (FPSC still), as illustrated in Figure 6d, except the cold seawater stream entering first into the solar thermal collector by using a water circulation pump (375 Watt) after opening the control valve (14) for preheating. The control valve (14) was left open until the cold seawater solution completely filled the copper collector's tube closing at the same time as the control valve (16). After the cold seawater solution filled the copper collector's tube and was heated up by absorbed solar radiation, the control valve (16) opened gradually to allow the preheated seawater solution to flow and fill the still basin with a tested depth; then, it closed once again. The above-mentioned steps were repeated until the collection of pure fresh water in the vessel.

Al_2O_3/seawater nanofluid with various nanoparticle concentrations is pushed through the solar collector's tube in order to remove the surplus heat produced by the flat-plate solar collector, as shown in Figure 6d. By providing direct contact continuous heating, the temperature of the surface of the pipe will be controlled by the Al_2O_3/seawater nanofluid, significantly improving the extraction of heat from the surface solar collector system. In Figure 6d, the hot Al_2O_3/seawater nanofluid is directed to the solar still (SS) unit for usage after leaving the solar collector. To achieve an accurate nanofluid mass flow rate, the rotameter is calibrated using the usual weighing approach with the assistance of a

stopwatch using the estimated nanofluid density, and the mass flow rate of the nanofluid is also obtained in the current study.

3.3. Solar Still Performance Parameters

(a) Solar still productivity (P_d)

The P_d of the solar still could be calculated by using Equations (32) and (33) [42,43].

$$P_d = \frac{Q_{e,w-gi} \times \Delta T}{L_w} \tag{32}$$

$$P_d = \frac{h_{e,w-gi} \times A_b \times \left(T_w - T_{gi}\right)}{L_w} \times 3.6 \tag{33}$$

where P_d is the hourly still productivity (kgh^{-1}), A_b is the basin surface area (m^2), ΔT is the temperature difference between the hot water and the cold glass cover (°C), $Q_{e,w-gi}$ is the evaporative heat transfer rate (Wm^{-2}), $h_{e,w-gi}$ is the evaporative heat transfer coefficient from the water surface to the glass cover (Wm^{-2} °C^{-1}), and L_w is the latent heat of water (≈2434 kJ kg^{-1}).

(b) Solar still thermal efficiency (η_{th})

The η_{th} of solar still could be determined mathematically using Equation (34) [42–45].

$$\eta_{th} = \frac{P_d \cdot L_w}{A_g \cdot I \cdot 3600} \times 100 \tag{34}$$

where L_w is the latent heat of water (J kg^{-1}) at average water temperature (T_w), A_g is the glass cover surface area (m^2), and I is the solar radiation incident on the glass cover surface (Wm^{-2}).

In case of single slope solar still with the support of a flat-plate solar collector (FPSC), the solar still thermal efficiency must consider the solar collector's energy gain as an energy entry. Its hourly thermal efficiency (η_{FPSC}) could be determined mathematically using Equations (35) and (36).

$$\eta_{FPSC} = \frac{P_d \cdot L_w}{\left[A_g \cdot I \cdot 3600\right] + Q_{ex}} \times 100 \tag{35}$$

$$Q_{ex} = m \cdot C \cdot \left(T_{in} - T_{out}\right) \times 100 \tag{36}$$

where Q_{ex} is the energy supplied by the nanofluid circulated in the copper tubes of solar collector to saline water (J/h), m is the flow rate of seawater with and without nanofluids (≈ 0.0075 kg/s), c is the specific heat of seawater with and without nanofluids (≈3959 and 3900 J/kg·K), and T_{in} and T_{out} are the inlet and outlet temperatures (°C), respectively, in the FPSC still with and without nanofluids in 1 h.

(c) Basin surface area (A_b)

The surface area of rectangular flat-plate-type still basin ($A_{b\text{-}flat}$) = Length × Width, while, in case of a v-corrugated-type still basin ($A_{b\text{-}corrugated}$) = area of one tunnel × number of tunnels (Figure 4).

3.4. Experimental Proceedings and Measurements

Experiments started at 7:00 h and continued up to 18:00 h during August 2022. The velocity of wind (W), ambient temperature (T_{ao}), and solar intensity (R) was measured experimentally using meteorological station (Vantage Pro 2, Davis, USA). Additionally, water (T_w), vapor (T_v), and inner glass cover (T_{gi}) temperatures are recorded by utilizing thermocouples (Lab-Jack logger, powered by USB cable, supply 5 volt, USA). The thermocouples are connected to a data-logger system to display and record the data during

the experimental period. The output data were recorded every five minutes and averaged every one hour during daylight.

4. Uncertainty Analysis

The features of each measuring instrumentation are shown together with the standard uncertainty in Table 3. According to [46], the usual standard uncertainty of each piece of equipment is defined using Equation (37).

$$u = a/\sqrt{3} \tag{37}$$

where a is the instrumentations accuracy [47,48].

Table 3. Instrumentation accuracy and uncertainty.

Instrumentations	Measurable Variable	Accuracy	Rang	Standard Uncertainty
Pyranometer	solar intensity	0.04 W/m^2	0–2300 W/m^2	2.36×10^{-2} W/m^2
Thermocouples	Nanofluid temperatures	±0.17 °C	(0–150) °C	7.3×10^{-2} °C
Infrared thermometer	SS surface temperature	±0.12 °C	(−10–200) °C	4.88×10^{-2} °C
Rotameter	Nanofluid flow rate	0.03 L/min	0.01–0.5 L/min	0.001 L/min

The uncertainty of the function X may be predicted if it is a function of 'n' independent linear parameters, as in $X = f(\beta 1, \beta 2, \ldots, \beta n)$ [49] using Equation (38).

$$\partial X = \sqrt{\left(\frac{\partial X}{\partial \beta_1}\partial\beta_1\right)^2 + \left(\frac{\partial X}{\partial \beta_2}\partial\beta_2\right)^2 + \cdots + \left(\frac{\partial X}{\partial \beta_n}\partial\beta_n\right)^2} \tag{38}$$

The maximum solar still productivity uncertainty, P_d, was determined using Equation (39) as the focal point.

$$P_d = f\left(h_{fg}, \Delta T, Q_{e,w-g}\right) = \pm\sqrt{\left(\frac{-\delta h_{fg}}{h_{fg}}\right)^2 + \left(\frac{\delta \Delta T}{\Delta T}\right)^2 + \left(\frac{\delta Q_{e,w-g}}{Q_{e,w-g}}\right)^2} = \pm 0.033 \tag{39}$$

The greatest error in the estimation of thermal efficiency was noted as 0.026, as detailed in Table 3.

The highest absolute uncertainty of the parameters was calculated to be less than 4%, showcasing the reliability of the assessed parameters.

5. Results and Discussion

5.1. Comparative Temperature Analysis of Solar Still Configurations

The hourly variations of basin water (T_w), inner glass cover (T_{gi}), and vapor (T_v) temperatures for conventional solar still (CSS), v-corrugated basin, reflecting mirror, FPSC still, and FPSC nanofluids are shown in Figure 7a–c. Investigations were carried out at an average ambient temperature of 30.9 °C, average solar radiation intensity of 506.9 W/m^2, water depth of 2 cm, and salt concentration of 33,162 ppm. The obtained results demonstrated that a v-corrugated basin, reflecting mirror, FPSC still, and FPSC nanofluids obviously upgraded the performance of the solar distillation unit in comparison with the conventional solar still (CSS). As shown in Figure 7a, the advanced basin water temperature (T_w) fulfilled with different enhancement techniques around the daytime compared to the conventional solar still (CSS) unit was associated mainly with a considerable increase in absorbed solar radiation and a heat loss reduction to the surrounding environment compared with conventional solar still (CSS) unit. The excessive energy losses took place in the case of a conventional solar still (CSS) unit, leading to a visible basin water temperature (T_w) decline. The enhanced basin water temperature (T_w) of a v-corrugated-type still basin was attributed to an increase in the surface area of heat and mass transfer (1.92 m^2) corresponding to only 1.04 m^2 in

the case of a flat-plate-type still basin of a conventional solar still (CSS) unit. Additionally, placing a mirror on the vertical side of the glass cover of the still helped in reflecting all the incoming solar radiation onto the seawater surface. As a result, this action elevated the temperature of the basin water (T_w). In the FPSC still and FPSC nanofluids, it was observed that the water temperature (T_w) consistently exceeded that of the conventional solar still (CSS) unit. This was attributed to a preheated water supply and a specific fin arrangement. The elevation in temperatures of the inner glass cover (T_{gi}), illustrated in Figure 7b, was predominantly attributable to distinct enhancement techniques applied during daylight hours. This rise was chiefly a consequence of a heightened rate of vapor condensation occurring on the interior glass cover surface, a phenomenon that differed significantly from the conventional solar still (CSS) unit. The use of FBSC nanofluid exhibited a significant increase in vapor temperature, reaching up to 100 degrees Celsius at 14:00, in contrast to the 70 degrees Celsius observed with the conventional CSS configuration (Figure 7c). As listed in Table 4, it was noted that a v-corrugated basin, reflecting mirror, FPSC still, and FPSC nanofluids completely affected the average basin water (T_w), inner glass cover (T_{gi}), and vapor (T_v) temperatures of the solar distillation unit. As an example, in comparison with the conventional solar still (CSS) unit, noticeable increases of around 11.53%, 22.45%, 33.89%, and 60.67% observed in average basin water temperature (T_w) for a v-corrugated basin, reflecting mirror, FPSC still, and FPSC nanofluids, respectively. Also, the average still glass cover temperature (T_{gi}) was raised by 6.96%, 16.46%, 25.14%, and 50.19% relative to the conventional solar still (CSS). Likewise, compared with the conventional solar still (CSS) unit, a v-corrugated basin, reflecting mirror, FPSC still, and FPSC nanofluids incremented the average vapor temperature (T_v) by nearly 12.38%, 23.22%, 33.79%, and 60.55%, respectively.

Table 4. The average basin water (T_w), inner glass cover (T_{gi}), vapor (T_v) temperatures in °C for different solar still configurations.

Various Solar Still Configurations	Average Different Temperatures (°C)		
	T_w	T_{gi}	T_v
CSS	54.03	42.95	51.57
v-corrugated basin still	60.72	45.94	57.52
Reflecting mirror still	66.58	50.02	63.15
FPSC still	72.29	53.75	69.05
FPSC nanofluids	86.75	64.51	82.86

5.2. Comparative Productivity Analysis of Solar Still Configurations

The resulting data presented in Figure 8 elucidated the impact of a v-corrugated basin, reflecting mirror, FPSC still, and FPSC nanofluids on the accumulated daily distillate productivity (P_d) of the solar distillation unit compared with a conventional solar still (CSS) unit. Figure 8 shows that a v-corrugated basin, reflecting mirror, FPSC still, and FPSC nanofluids greatly enhanced the still daily productivity (P_d) by roughly 22.39%, 41.72%, 70.10%, and 104.13%, respectively, compared with the conventional solar still (CSS) unit. The improved accumulated daily distillate productivity (P_d) was ascribed to a considerable augmentation in the temperature difference between the hot water and the cold glass cover ($\Delta T_{w\text{-}gi}$) by around 34.33%, 52.32%, 77.37%, and 112.87% on average around the daytime compared to the unit of a conventional solar still (CSS), in which a high thermal capacity was the main reason for a productivity (P_d) decrease, as illustrated in Figure 9. Additionally, the improved accumulated daily productivity (P_d) in the case of the FPSC still and FPSC nanofluids could be translated by increasing the heat transfer rate from the hot water surface to the inner cold glass cover surface via convective, evaporative, and radiative forces.

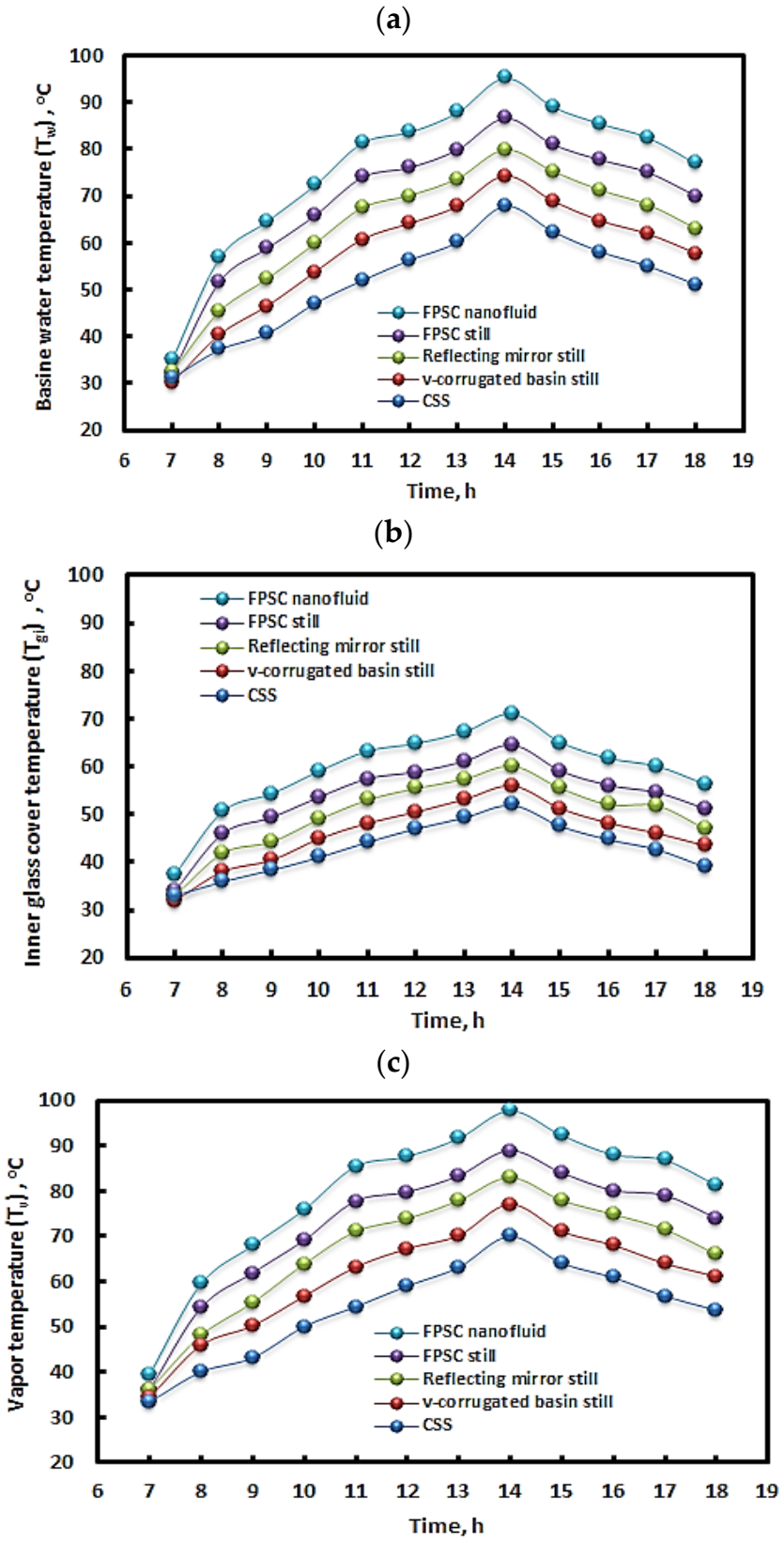

Figure 7. The hourly variation of basin water, inner glass cover, vapor temperatures for different solar still configurations (**a**) Time vs. basin water temperature, (**b**) Time vs. inner glass cover temperature and (**c**)Time vs. vapour temperature.

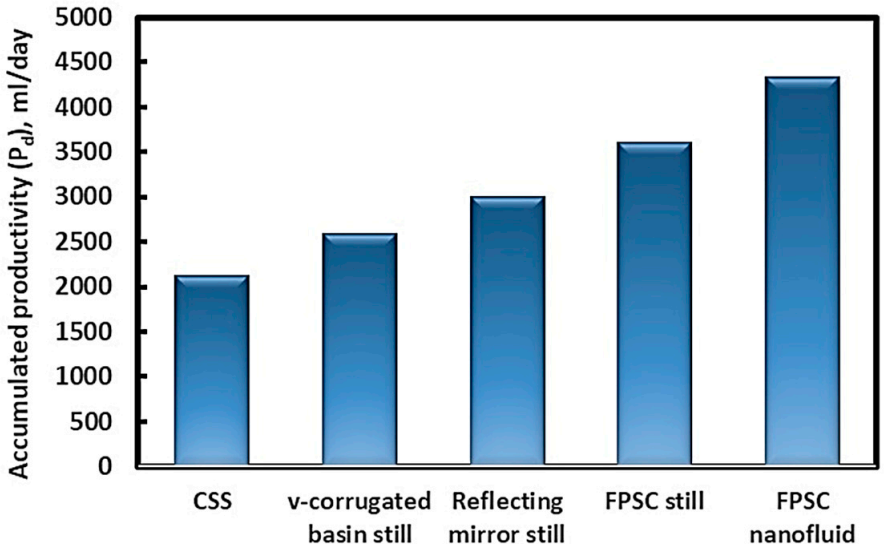

Figure 8. Assessing the daily productivity (P_d) of various solar still configurations under atmospheric conditions from June to August.

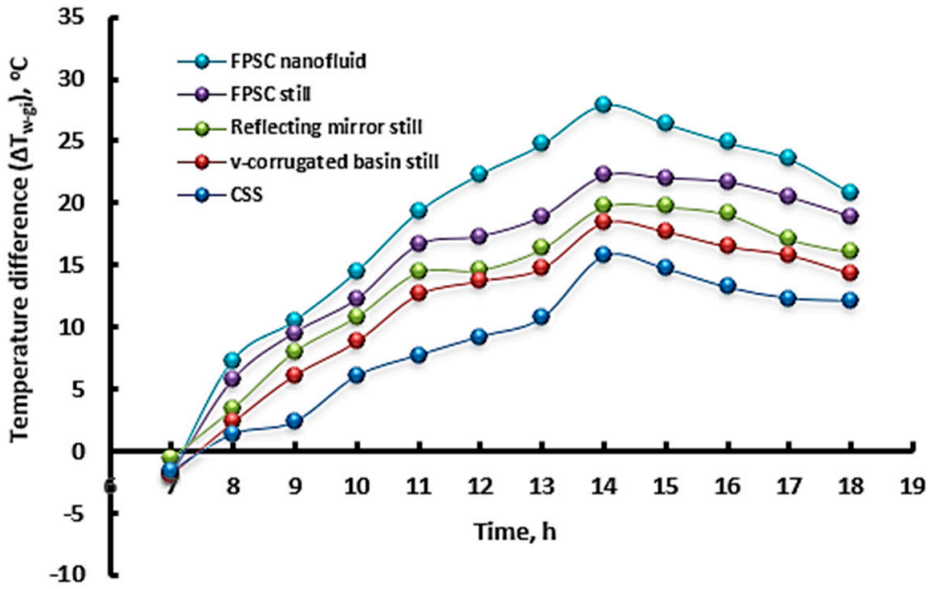

Figure 9. The hourly variation of the temperature difference (ΔT_{w-gi}) for different solar still configurations.

5.3. Comparative Thermal Efficiency Analysis of Solar Still Configurations

Figure 10 displays that the positive influence of a v-corrugated basin, reflecting mirror, FPSC still, and FPSC nanofluids for the average daily thermal efficiency (η) is 22.01%, 26.71%, 39.57%, and 56.21%, respectively. The achieved augmentation in the average thermal efficiency (η) could be explained due to two reasons: firstly, increasing water evaporation and condensation processes thanks to various improvement techniques contrasted to the conventional solar still (CSS); secondly, a large amount of thermal energy added during sunshine hours until sunset by virtue of integrating the solar thermal collector into the solar distillation unit. Meanwhile, a decline happened in the average thermal efficiency (η) of a conventional solar still (CSS) unit, attributed mainly to a high specific heat capacity and lower distillate productivity (P_d).

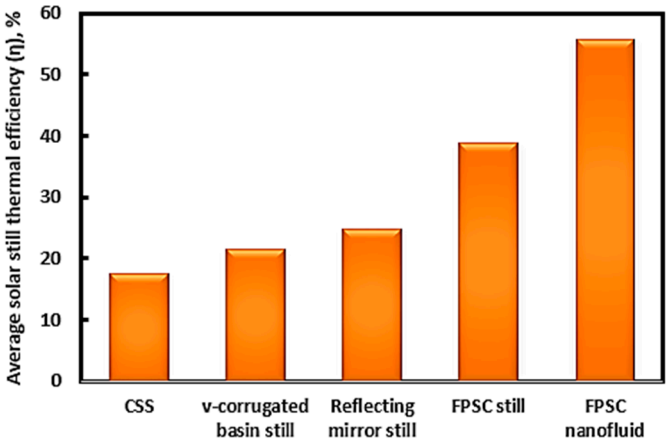

Figure 10. Comparison of the average daily thermal efficiency (η_{th}) for different solar still configurations.

6. Comparative Assessment with Current Study

Table 5 presents comparisons of productivity (P_d) and thermal efficiency (η) between the single slope solar still tested in the current experimental study and previous solar still unit studies. The utilization of Al_2O_3 water-based nanofluid in the solar collector (FPSC) within this study demonstrated a notable and substantial enhancement in both thermal efficiency (56.21%) and productivity (104.13%) when compared to previous research. The incorporation of Al_2O_3 nanoparticles into the water-based nanofluid significantly augmented the heat transfer characteristics within the collector. This enhancement can be attributed to the improved thermal conductivity and convective heat transfer properties of the nanofluid, facilitating better heat absorption and transfer within the system. Consequently, the increased thermal efficiency of the solar collector led to a substantial improvement in the overall productivity of the system. The findings suggest that employing Al_2O_3 water-based nanofluid in the solar collector configuration represents a promising advancement, offering an effective means to significantly enhance both thermal efficiency and productivity, thus contributing to the potential advancement of solar energy utilization for various applications.

Table 5. A comparative study between the current investigation and previous studies on solar distillation techniques, including V-corrugated basin, reflecting mirror, FPSC still, and FPSC nanofluids.

References	Various Enhancements of Solar Still Configurations	Improvement in Productivity (%)	Thermal Efficiency (%)	Operating Conditions
Current study	V-corrugated basin	22.39	22.01	Average T_{ao} = 30.9 °C, average I = 506.9 W/m^2, water depth = 2 cm, Seawater salinity = 33,162 ppm, single slope solar still.
	Internal reflecting mirror	41.72	26.71	
	FPSC still	70.10	39.57	
	FPSC nanofluids (Al_2O_3/water)	104.13	56.21	
[9]	V-corrugated basin	21	41	Wind speed = 0.4 to 4.3 m/s, solar intensity = 20 to 1100 W/m^2. Water depth = 50 mm, quantity of saline water =30 and 50 L, single slope solar still.
[50]	Internal reflecting mirror	75	56	Saline water depth = 5 mm, stepped solar still.
[11]	FPSC still	20.8	20.4	Fresh tap water, V-shaped glass solar still.
		24.1	23.6	Saline water concentration = 5%, V-shaped glass solar still.

Table 5. *Cont.*

References	Various Enhancements of Solar Still Configurations	Improvement in Productivity (%)	Thermal Efficiency (%)	Operating Conditions
[13]	FPSC still	36	--	Water depth = 2 cm, single slope solar still.
[45]	Fresnel lens concentrator nanofluids (Al_2O_3–Therminol-55 nanofluid (nHTF))	--	53.55	Flow rate of nHTF = 0.5 L/min, saline water depth = 25 mm, solar intensity = 764 to 770 W/m^2, single slope solar still.
[51]	Blackened stainless steel balls: 1. 10 mm diameter	38.07	27.81	Brackish water salinity = 1850 ppm, water depth = 15 mm, single slope solar still.
	2. 5 mm diameter	31.41	26.56	
	Internal reflecting aluminum foils	14.87	23.32	
[52]	Nano Fe_2O_3 particles (NALSS)	53.49	30.76	Ferric oxide density = 5.24 g/cm^3, solar irradiation varied from 125 to 712 W/m^2, water depth = 0.5 cm, single slope solar still.
[53]	Different heat localization materials: 1. (HSHLM)-exfoliated graphite flakes with wick (Type A)	34.48	37.68	Maximum solar irradiation = 950 W/m^2 (at 12:30 p.m.), average air temperature = 32 °C, saline water from Mediterranean Sea, water depth = 1 cm, single slope solar still.
	2. (HSHLM)-carbon foam with wick (Type B)	28.57	28.89	Maximum solar irradiation = 945 W/m^2 (at 12:30 p.m.), average air temperature = 25 °C, saline water from Mediterranean Sea, water depth = 1 cm, single slope solar still.
	3. (HSHLM)-exfoliated graphite flakes with wick and carbon foam (Type C)	51.78	47.24	Maximum solar irradiation = 970 W/m^2 at 12:30 p.m., average air temperature = 31 °C saline water from Mediterranean Sea, water depth = 1 cm, single slope solar still.
[54]	Various corrugated absorber shapes: 1. Flat absorber (HSD-FA)	16.67	--	Brine water, water depth = 1.5 cm, average solar intensity = 654 W/m^2, average climate temperatures = 38.9 °C, hemispherical solar still (HSD).
	2. Square corrugated absorber (HSDSA)	27.08	--	
	3. Semi-circular corrugated absorber (HSDSCA)	39.58	--	
	4. Triangular corrugated absorber (HSDTA)	48.96	--	
[55]	1. V-corrugated iron tray HSD	42.85	48.28	Average solar intensity = 619.3 W/m^2, average air temperature = 38.2 °C, and hemispherical solar still (HSD).
	2. Flat iron tray HSD	14.30	38.72	
	3. Wick materials with v-corrugated iron tray	83.12	61.67	
	4. Wick materials with flat tray	--	52.16	

Table 5. *Cont.*

References	Various Enhancements of Solar Still Configurations	Improvement in Productivity (%)	Thermal Efficiency (%)	Operating Conditions
[56]	Different porous absorbing materials: 1. Natural luffa fiber (NLF)	56.14	21.22	The solar radiation ranged from 400 to 995 W/m^2, seawater salinity = 15,300 ppm, single slope solar still.
	2. Black luffa fiber (BLF)	77.61	24.71	
	3. Fine steel wool (FSW)	98.29	28.60	
	4. Steel wool pads (SWP)	134.18	32.74	
[57]	Thermal CPC collector, photovoltaic panel, TES (quartz sand) and distiller basin material (tarnished copper)	91	--	Maximum solar irradiation of 845 W/m^2 at 12 p.m., average air temperature = 18 °C, seawater mass of 35 kg, single slope solar still.
[58]	Various energy storage materials: 1. 5 kg of fine sand (0.125–0.25-mm grain size)	--	50.69	Average solar irradiance = 680, 683, and 689 W/m^2, daily average ambient temperature during the experimentations is between 35 and 37 °C, water depth = 0.5 cm, tubular solar still (TSS).
	2. Small gravels (20–30 mm)	--	61.13	
	3. Black granite (5-mm thickness)	10.5 (compared to gravel) 32.3 (compared to sand)	67.09	

7. Conclusions

In the current work, a v-corrugated basin, reflecting mirror, FPSC still, and FPSC nanofluids deeply improved the solar still distillate productivity (P_d) and thermal efficiency (η_{th}) compared with a conventional solar still (CSS) unit. This was owing to significantly increasing the temperature difference between the two hot water and cold glass cover surfaces ($\Delta T_{w\text{-}gi}$). Under an average ambient temperature of 30.9 °C, average solar radiation intensity of 506.9 W/m^2, water depth of 2 cm, and salt concentration of 33,162 ppm, the solar still distillate productivity (P_d) was upgraded by nearly 22.39%, 41.72%, 70.10%, and 104.13% by virtue of a v-corrugated basin, reflecting mirror, FPSC still, and FPSC nanofluids, respectively, compared with the conventional solar still (CSS) unit. This was ascribed to a considerable augmentation in the temperature difference between the two hot water and cold glass cover surfaces ($\Delta T_{w\text{-}gi}$) by around 34.33%, 52.32%, 77.37%, and 112.87%, respectively, compared with the conventional solar still (CSS), in which a high thermal capacity leads to a productivity (P_d) decrease. Also, the v-corrugated basin, reflecting mirror, FPSC still, and FPSC nanofluids greatly upgraded the average solar still thermal efficiency (η_{th}) by about 22.01%, 26.71%, 39.57%, and 56.21%, respectively. The results demonstrated that integrating a v-corrugated basin, reflecting mirror, FPSC still, and FPSC nanofluids into combined active solar distillation units significantly enhanced the performance of the solar distillation unit. These combined configurations effectively raised the temperature of the basin water (T_w) and increased the temperature difference between the hot water and the inner cold glass cover surfaces ($\Delta T_{w\text{-}gi}$), thereby resulting in improved performance of the solar still.

Author Contributions: Conceptualization, Y.E., S.S.K., M.A.-R.A.-Z. and M.B.; Methodology, M.A.-R.A.-Z., Y.E., M.T., M.B., T.M., O.A.A.-Q. and S.S.K.; Software, M.A.-R.A.-Z. and S.S.K.; Validation, M.A.-R.A.-Z., Y.E., M.T., M.B., O.A.A.-Q. and S.S.K.; Formal analysis, M.A.-R.A.-Z.; Investigation, M.A.-R.A.-Z., Y.E., M.T., M.B., T.M., O.A.A.-Q. and S.S.K.; Resources, O.A.A.-Q.; Writing—review & editing, T.M. All authors have read and agreed to the published version of the manuscript.

Funding: This research received no external funding.

Institutional Review Board Statement: Not applicable.

Informed Consent Statement: Not applicable.

Data Availability Statement: Data will be available from the corresponding author on request.

Acknowledgments: The researchers would like to acknowledge the assistance provided by the Science and Technology Development Fund (STDF) for funding the project, No. 41902 (Center of Excellence in Membrane-based Water Desalination Technology for Testing and Characterization).

Conflicts of Interest: The authors declare no conflict of interest.

Nomenclature

a	Accuracy of instrument
A_b	Basin surface area (m^2)
A_g	Glass cover surface area (m^2)
A_w	Water surface area (m^2)
C_{pw}	Specific heat of seawater (J/kg·K)
C_{pb}	Basin specific heat (J/kg·K)
C_{pg}	Glass cover specific heat (J/kg·K)
F_c	Convective fraction
F_e	Evaporative fraction
F_r	Radiative fraction
K	Thermal conductivity (W/m.K)
k_g	Glass cover thermal conductivity (W/m.K)
k_{in}	Insulation thermal conductivity (W/m.K)
n	Particle shape factor
I	Solar radiation flux incident on the basin (Wm^{-2})
L_w	Latent heat of vaporization (kJ kg^{-1})
m	Flow rate of seawater with and without nanofluids (kg/s)
m_b	Basic mass (kg)
m_c	Mass of condensated water (kg)
m_g	Mass of the glass cover (kg)
m_w	Water mass (kg)
Q_{ex}	Energy supplied by the nanofluid circulated in the copper tubes of solar collector to saline water (J/h)
$Q_{e,w-gi}$	Evaporative heat transfer rate within still from the water surface to the interior surface of the glass cover (Wm^{-2})
q_b	Conductive heat transfer rate from the basin bottom to the atmosphere (Wm^{-2})
q_{bwb}	Convective heat transfer rate from the black basin liner to the water surface (Wm^{-2})
q_{cga}	Convective heat transfer rate from the exterior surface of the glass cover to the atmosphere (Wm^{-2})
q_{cw}	Convective heat transfer rate within still from the water surface to the interior surface of the glass cover (Wm^{-2})
q_{rgs}	Radiative heat transfer rate from the exterior surface of the glass cover to the sky (Wm^{-2})
q_{rwb}	Radiative heat transfer rate within still from the water surface to the interior surface of the glass cover (Wm^{-2})
q_1	Total value of the energy transfer within the still from the water surface to the interior surface of the glass cover (Wm^{-2})
q_2	Total value of the energy transfer from the exterior surface of the glass cover to the atmosphere (Wm^{-2})
h_{bw}	Convective heat transfer coefficient from the black basin liner to the water surface (Wm^{-2} $°C^{-1}$)
h_{cga}	Convective heat transfer coefficient from the exterior surface of the glass cover to the atmosphere (Wm^{-2} $°C^{-1}$)
h_{cw}	Convective heat transfer coefficient from water surface to the interior surface of the glass cover (Wm^{-2} $°C^{-1}$)
h_{ew}	Evaporative heat transfer coefficient from water surface to the interior surface of the glass cover (Wm^{-2} $°C^{-1}$)
$h_{e,w-gi}$	Evaporative heat transfer coefficient from water surface to glass cover (Wm^{-2} $°C^{-1}$)

h_{rgs}	Radiative heat transfer coefficient from the exterior surface of the glass cover to the sky ($Wm^{-2}\ ^{\circ}C^{-1}$)
h_{rw}	Radiative heat transfer coefficient from the water surface to the interior surface of the glass cover ($Wm^{-2}\ ^{\circ}C^{-1}$)
h_1	Total internal heat transfer coefficient from the water surface to the interior surface of the glass cover ($Wm^{-2}\ ^{\circ}C^{-1}$)
h_2	Total external heat transfer coefficient from the exterior surface of the glass cover to the atmosphere ($Wm^{-2}\ ^{\circ}C^{-1}$)
T_w	Basin water temperature (°C)
T_{in}	Inlet temperature in the FPSC still with and without nanofluids in 1 h (°C)
T_{out}	Outlet temperature in the FPSC still with and without nanofluids in 1 h (°C)
T_{ao}	Ambient temperature (°C)
T_v	Vapor temperature (°C)
T_{sky}	Sky temperature (°C)
T_{go}	Outer glass cover temperature (°C)
T_{gi}	Inner glass cover temperature (°C)
u	Standard uncertainty
$\Delta T_{w\text{-}gi}$	Temperature difference between the hot basin water surface and the interior cooling glass cover surface (°C)
U_g	Conductive heat transfer coefficient through the thickness of the still cover $Wm^{-2}\ ^{\circ}C^{-2}$
W	Vel°City of wind (m/sec)
x_g	Glass cover thickness (m/s)
x_{in}	Insulation thickness (m/sec)
P_d	Hourly condensate (distillate) production from the still (kgh^{-1})
P_{gi}	Partial pressure of water vapor at inner glass temperature within the still (Nm^{-2})
P_{wb}	Partial pressure of water vapor at water temperature within the still (Nm^{-2})
Abbreviations	
SS	Solar still
CSS	Conventional solar still
MSS	Modified solar still
FPSC	Flat-plate solar collector
HDH	Humidification-dehumidification
MSF	Multi-stage flash
MED	Multi-effect distillation
VC	Vapor compression
Subscripts	
bf	base fluid
nf	nanofluid
p	nanoparticle
u	useful
Greek letters	
η_{th}	Solar still thermal efficiency (%)
η_{FPSC}	Solar still-solar collector thermal efficiency (%)
ρ	Density of fluid (kg/m^3)
ϕ	Concentration ratio by volume of nanoparticles
ε_{eff}	Shape factor of diffuse radiation between the water surface and the glass cover (effective emissivity)
σ	Stefan -Boltzmann constant ($Wm^{-2}\ K^{-4}$)

References

1. Ibrahim, A.G.M.; Elshamarka, S.E. Performance study of a modified basin type solar still. *Sol. Energy* **2015**, *118*, 397–409. [CrossRef]
2. Elbany, M.; Elhenawy, Y. Analyzing the ultimate impact of COVID-19 in Africa. *Case Stud. Transp. Policy* **2021**, *9*, 796–804. [CrossRef]
3. Sharshir, S.W.; Yang, N.; Peng, G.; Kabeel, A.E. Factors affecting solar stills productivity and improvement techniques: A detailed review. *Appl. Therm. Eng.* **2016**, *100*, 267–284. [CrossRef]

4. Shukla, S.K.; Sorayan, V.P.S. Thermal modeling of solar stills: An experimental validation. *Renew. Energy* **2005**, *30*, 683–699. [CrossRef]
5. Kabeel, A.E.; Hamed, A.M.; El-Agouz, S.A. Cost analysis of different solar still configurations. *Energy* **2010**, *35*, 2901–2908. [CrossRef]
6. Al-Hayek, I.; Badran, O.O. The effect of using different designs of solar stills on water distillation. *Desalination* **2004**, *169*, 121–127. [CrossRef]
7. Chan, W.W.; Jiang, B.; Liu, L. Comparative studies of solar collectors in southern China hotels. *J. China Tour. Res.* **2013**, *9*, 292–304. [CrossRef]
8. Tanaka, H. Monthly optimum inclination of glass cover and external reflector of a basin type solar still with internal and external reflector. *Sol. Energy* **2010**, *84*, 1959–1966. [CrossRef]
9. Omara, Z.M.; Hamed, M.H.; Kabeel, A.E. Performance of finned and corrugated absorbers solar stills under Egyptian conditions. *Desalination* **2011**, *277*, 281–287. [CrossRef]
10. Eltawil, M.A.; Omara, Z.M. Enhancing the solar still performance using solar photovoltaic, flat plate collector and hot air. *Desalination* **2014**, *349*, 1–9. [CrossRef]
11. Sheeba, K.N.; Babu, J.S.-C.; Jaisankar, S. Performance evaluation of a flat plate collector coupled solar still system. *Energy Sources Part A Recovery Util. Environ. Eff.* **2015**, *37*, 291–298. [CrossRef]
12. Rai, S.N.; Tiwari, G. Single basin solar still coupled with flat plate collector. *Energy Convers. Manag.* **1983**, *23*, 145–149. [CrossRef]
13. Badran, O.O.; Al-Tahaineh, H.A. The effect of coupling a flat plate collector on the solar still productivity. *Desalination* **2005**, *183*, 137–142. [CrossRef]
14. Badran, O.O. Experimental study of the enhancement parameters on a single slope solar still productivity. *Desalination* **2007**, *209*, 136–143. [CrossRef]
15. Tanaka, H. Experimental study of a basin type solar still with internal and external reflectors in winter. *Desalination* **2009**, *249*, 130–134. [CrossRef]
16. Hiroshi, T.; Yasuhito, N. Theoretical analysis of a basin type solar still with internal and external reflectors. *Desalination* **2006**, *197*, 205–216.
17. Omara, Z.M.; Kabeel, A.E.; Younes, M.M. Enhancing the stepped solar still performance using internal and external reflectors. *Energy Convers. Manag.* **2014**, *78*, 876–881. [CrossRef]
18. Omara, Z.M.; Kabeel, A.E.; Abdullah, A.S.; Essa, F.A. Experimental investigation of corrugated absorber solar still with wick and reflectors. *Desalination* **2016**, *381*, 111–116. [CrossRef]
19. Abdallah, S.; Badran, O.; Mazen, M.; Khader, A. Performance evaluation of a modified design of a single slope solar still. *Desalination* **2008**, *219*, 222–230. [CrossRef]
20. Hameed, H.G.; Diabil, H.A.N.; Al-Fahham, M.A. Performance study on a solar concentrator system for water distillation using different water nanofluids. *Heliyon* **2023**, *9*, e16535. [CrossRef]
21. Zakaria, M.; Sharaky, A.M.; Al-Sherbini, A.-S.; Bassyouni, M.; Rezakazemi, M.; Elhenawy, Y. Water desalination using solar thermal collectors enhanced by nanofluids. *Chem. Eng. Technol.* **2022**, *45*, 15–25. [CrossRef]
22. Fouad, K.; Alalm, M.G.; Bassyouni, M.; Saleh, M.Y. A novel photocatalytic reactor for the extended reuse of W–TiO2 in the degradation of sulfamethazine. *Chemosphere* **2020**, *257*, 127270. [CrossRef] [PubMed]
23. Abu-Arabi, M.; Zurigat, Y.; Al-Hinai, H.; Al-Hiddabi, S. Modeling and performance analysis of a solar desalination unit with double-glass cover cooling. *Desalination* **2002**, *143*, 173–182. [CrossRef]
24. Baum, V.A.; Bairamov, R. Heat and mass transfer processes in solar stills of hot-box type. *Sol. Energy* **1964**, *8*, 78. [CrossRef]
25. Dunkle, R.V. Solar water distillation: The roof-type still and a multiple- effect diffusion still. In *International Developments in Heat Transfer, ASME, Proceedings International Heat Transfer Part V*; University of Colorado: Victoria, Australia, 1961; p. 895.
26. Fernandez, J.L.; Chargoy, N. Multi stage indirectly heated solar still. *Sol. Energy J.* **1990**, *44*, 215–223. [CrossRef]
27. Duffie, J.A.; Beckman, W.A. *Solar Engineering of the Thermal Process*; Wiley: New York, NY, USA, 1991; pp. 3–44.
28. Tiwari, A.K.; Tiwari, G.N. Thermal modeling based on solar fraction and experimental study of the annual and seasonal performance of a single slope passive solar still: The effect of water depths. *Desalination* **2007**, *207*, 184–204. [CrossRef]
29. Cooper, P.I. Digital simulation of experimental solar still data. *Sol. Energy* **1973**, *14*, 451. [CrossRef]
30. Sartori, E. Solar still versus solar evaporator: A comparison study between their thermal behaviors. *Sol. Energy* **1996**, *56*, 199–206. [CrossRef]
31. McAdams, W.H. *Heat Transmission*, 3rd ed.; McGraw-Hill Book Company: New York, NY, USA, 1954.
32. Swinbank, Long-wave radiation from clear skies. *Q. J. R. Meteorol. Soc.* **1963**, *89*, 339–348. [CrossRef]
33. Rai, G.D. *Solar Energy Utilization. A Text Book for Engineering Students*; Some additional methods of solar energy utilization; Khanna: Delhi, India, 1980; Chapter 12; pp. 194–197.
34. Hamdan, M.A.; Musa, A.M.; Jubran, B.A. Performance of solar still under Jordanian climate. *Energy Conserv. Manag.* **1999**, *40*, 495–503. [CrossRef]
35. Ebaid, M.S.; Al-busoul, M.; Ghrair, A.M. Performance enhancement of photovoltaic panels using two types of nanofluids. *Heat Transf.* **2020**, *49*, 2789–2812. [CrossRef]

36. Sardarabadi, M.; Hosseinzadeh, A.; Kazemian, M. Passandideh-Fard, Experimental investigation of the effects of using metal-oxides/water nanofluids on a photovoltaic thermal system (PVT) from energy and exergy viewpoints. *Energy* **2017**, *138*, 682–695. [CrossRef]
37. Michael, J.J.; Iniyan, S. Performance analysis of a copper sheet laminated photovoltaic thermal collector using copper oxide–water nanofluid. *Sol. Energy* **2015**, *119*, 439–451. [CrossRef]
38. Sharaf, O.Z.; Orhan, M.F. Thermodynamic analysis and optimization of densely-packed receiver assembly components in high-concentration CPVT solar collectors. *Energy Convers. Manag.* **2016**, *121*, 113–144. [CrossRef]
39. Poredoš, P.; Tomc, U.; Petelin, N.; Vidrih, B.; Flisar, U.; Kitanovski, A. Numerical and experimental investigation of the energy and exergy performance of solar thermal, photovoltaic and photovoltaic-thermal modules based on roll-bond heat exchangers. *Energy Convers. Manag.* **2020**, *210*, 112674. [CrossRef]
40. Radwan, A.; Ahmed, M.; Ookawara, S. Performance enhancement of concentrated photovoltaic systems using a microchannel heat sink with nanofluids. *Energy Convers. Manag.* **2016**, *119*, 289–303. [CrossRef]
41. Sardarabadi, M.; Passandideh-Fard, M.; Heris, S.Z.J. Experimental investigation of the effects of silica/water nanofluid on PV/T (photovoltaic thermal units). *Energy* **2014**, *66*, 264–272. [CrossRef]
42. Gupta, B.; Mandraha, T.; Edla, P.; Pandya, M. Thermal modeling and efficiency of solar water distillation: A review. *Am. J. Eng. Res.* **2013**, *2*, 203–213.
43. Manokar, A.; Vimala, M.; Winston, D.; Ramesh, R.; Sathyamurthy, R.; Nagarajan, P.; Bharathwaaj, R. Different parameters affecting the condensation rate on an active solar still—A review. *Env. Prog. Sustain. Energy* **2019**, *38*, 286–296. [CrossRef]
44. Mabrouk, A.N.; Elhenaw, Y.; Abdelkader, M.; Shatat, M. The impact of baffle orientation on the performance of the hollow fiber membrane distillation. *Desalination Water Treat.* **2017**, *58*, 35–45. [CrossRef]
45. Muraleedharan, M.; Singh, H.; Udayakumar, M.; Suresh, S. Modified active solar distillation system employing directly absorbing Therminol 55–Al2O3 nano heat transfer fluid and Fresnel lens concentrator. *Desalination* **2019**, *457*, 32–38. [CrossRef]
46. Elhenawy, Y.; Moustafa, G.H.; Attia, A.M.; Mansi, A.E.; Majozi, T.; Bassyouni, M. Performance enhancement of a hybrid multi effect evaporation/membrane distillation system driven by solar energy for desalination. *J. Environ. Chem. Eng.* **2022**, *10*, 108855. [CrossRef]
47. Gupta, S.V. *Measurement Uncertainties: Physical Parameters and Calibration of Instruments*; Springer Science & Business Media: Berlin/Heidelberg, Germany, 2012.
48. Kirkup, L.; Frenkel, R.B. *An Introduction to Uncertainty in Measurement: Using the GUM (Guide to the Expression of Uncertainty in Measurement)*; Cambridge University Press: Cambridge, UK, 2006.
49. Alhathal Alanezi, A.; Bassyouni, M.; Abdel-Hamid, S.M.; Ahmed, H.S.; Abdel-Aziz, M.H.; Zoromba, M.S.; Elhenawy, Y. Theoretical investigation of vapor transport mechanism using tubular membrane distillation module. *Membranes* **2021**, *11*, 560. [CrossRef]
50. Omara, Z.M.; Kabeel, A.E.; Younes, M.M. Enhancing the stepped solar still performance using internal reflectors. *Desalination* **2013**, *314*, 67–72. [CrossRef]
51. Diabil, H.A.N. Experimental study to enhance the productivity of single-slope single-basin solar still. *Open Eng.* **2022**, *12*, 157–168. [CrossRef]
52. Balachandran, G.B.; David, P.W.; Mariappan, R.K.; Kabeel, A.E.; Athikesavan, M.M.; Sathyamurthy, R. Improvising the efficiency of single-sloped solar still using thermally conductive nano-ferric oxide. *Environ. Sci. Pollut. Res.* **2020**, *27*, 32191–32204. [CrossRef] [PubMed]
53. Sharshir, S.W.; Elsheikh, A.H.; Ellakany, Y.M.; Kandeal, A.W.; Edreis, E.M.A.; Sathyamurthy, R.; Thakur, A.K.; Eltawil, M.A.; Hamed, M.H.; Kabeel, A.E. Improving the performance of solar still using different heat localization materials. *Environ. Sci. Pollut. Res.* **2020**, *27*, 12332–12344. [CrossRef]
54. Kabeel, A.E.; Attia, M.E.H.; Bellila, A.; El-Maghlany, W.M.; Fayed, M.; Abdullah, A.S.; Zidane, I.F. The impact of the corrugated absorber shape on the performance of a hemispherical solar still for water desalination: An experimental study. *Appl. Water Sci.* **2023**, *13*, 108. [CrossRef]
55. Attia, M.E.H.; Zayed, M.; Abdelgaied, M.; Sharshir, S.; Kabeel, A.E.; Abdalla, A. Experimental investigation on a modified design of hemispherical solar distiller with v-corrugated iron trays and wick materials for improving freshwater production. *Environ. Sci. Pollut. Res.* **2022**, *29*, 83756–83769. [CrossRef]
56. Ramzy, K.; Abdelgaleel, M.; Kabeel, A.E.; Mosalam, H. Performance of a single slope solar still using different porous absorbing materials: An experimental approach. *Environ. Sci. Pollut. Res.* **2023**, *30*, 72398–72414. [CrossRef]
57. Bellatreche, R.; Ouali, M.; Balistrou, M.; Tassalit, D. Thermal efficiency improvement of a solar desalination process by parabolic trough collector. *Water Supply* **2021**, *21*, 3698–3709. [CrossRef]
58. Sambare, R.K.; Dewangan, S.K.; Gupta, P.K.; Joshi, S. Augmenting the productivity of tubular solar still using low-cost energy storage materials. *Environ. Sci. Pollut. Res.* **2022**, *29*, 78739–78756. [CrossRef] [PubMed]